Catalysis Science & Technology

ROYAL SOCIETY OF CHEMISTRY

PAPER

View Article Online
View Journal | View Issue

Open Access Article. Published on 22 March 2023. Downloaded on 2/20/2026 7:25:29 PM.
This article is licensed under a Creative Commons Attribution-NonCommercial 3.0 Unported Licence.

Check for updates

Cite this: *Catal. Sci. Technol.*, 2023, **13**, 2748

Understanding W/H-ZSM-5 catalysts for the dehydroaromatization of methane†

Mustafa Çağlayan,[a] Abdallah Nassereddine,[b] Stefan-Adrian F. Nastase,[c] Antonio Aguilar-Tapia,[d] Alla Dikhtiarenko,[a] Sang-Ho Chung,[e] Genrikh Shterk,[a] Tuiana Shoinkhorova,[a] Jean-Louis Hazemann,[b] Javier Ruiz-Martinez,[e] Luigi Cavallo,[c] Samy Ould-Chikh[c] and Jorge Gascon*[a]

Received 19th January 2023,
Accepted 22nd March 2023

DOI: 10.1039/d3cy00103b

rsc.li/catalysis

Tungsten is the most interesting and promising metal to replace molybdenum in methane dehydroaromatization (MDA) catalysis. Located in the same column of the periodic table, tungsten displays similar chemical features to molybdenum (*i.e.*, formation and stability of oxidation states, acidity of trioxides, tendency toward formation of polynuclear species, atomic radii, ionic radii, *etc.*) but shows higher thermal stability. The latter could be an advantage during high-temperature reaction–regeneration cycles. However, the MDA activity of W–ZSM-5 catalysts is much lower than the activity obtained with their Mo counterpart. In order to gain a further understanding of such differences in catalytic activity, we present a thorough investigation of the effect of dispersion and distribution of W sites on the zeolite, their relation with catalytic activity, and the temporal evolution of dispersion with reaction–regeneration cycles. The structure of W sites is elucidated with advanced and detailed characterization techniques, including *operando* X-ray absorption spectroscopy (XAS). The information obtained can help the catalysis community to design better W catalysts for MDA and other reactions (*i.e.*, metathesis, hydrocarbon cracking, hydrodesulfurization, isomerization, *etc.*) where this is the metal of choice.

Introduction

In today's world, increasing methane emissions[1] and high transportation-storage costs of natural gas[2] (compared to other fossil fuels) make on-site methane conversion into condensed phase chemicals a prominent topic in catalysis science. Despite the commercialized indirect technologies (*i.e.*, through steam-reforming reaction to methanol synthesis or Fischer–Tropsch synthesis) to incorporate natural gas into the existing petrochemical infrastructure, there is still an intense desire to develop catalytic processes that would convert methane to value-added chemicals and fuels in one single step. In this spirit, the non-oxidative methane dehydroaromatization (MDA, $6CH_4 = C_6H_6 + 9H_2$, $\Delta H_{998K} = 598.4$ kJ mol^{-1}) over metal-incorporated zeolite catalysts remains of high interest among catalysis science researchers, who are trying to gain insight into the direct methane valorization and further improve the process despite its inherent challenges (*i.e.*, thermodynamic limitations, high coke selectivity, quick catalyst deactivation).

Since the discovery of MDA activity of Mo-loaded ZSM-5 catalyst,[3] several different transition metals (W, Fe, Cr, V, Re, *etc.*)[4] and zeolites (MCM-41, ZSM-8, TNU-9, MOR, SSZ-13, *etc.*)[5] were utilized and investigated. Yet, the best combination for high MDA activity is still Mo/H-ZSM-5. Consequently, many researchers – including us – have focused on Mo/H-ZSM-5 catalysts intensively to understand the formation of active Mo sites and the reaction mechanism.[6–10] Since the aromatization feature of MFI topology is well-known for many zeolite-catalyzed reactions (*i.e.*, methanol-to-hydrocarbons,[11] aliphatics aromatization,[12] *etc.*), further investigations on the zeolite fragment (topologies) of the catalyst may not be the prioritized research topic. However, there is still a gap of understanding for other metallozeolite catalysts; highlighting the importance of more research to address unresolved fundamental issues (*i.e.*, nature of active catalytic sites) and

[a] KAUST Catalysis Center (KCC), Advanced Catalytic Materials, King Abdullah University of Science and Technology (KAUST), Thuwal 23955, Saudi Arabia. E-mail: jorge.gascon@kaust.edu.sa
[b] Institut Néel, UPR 2940 CNRS – Université Grenoble Alpes, Grenoble F-38000, France
[c] KAUST Catalysis Center (KCC), King Abdullah University of Science and Technology (KAUST), Thuwal 23955, Saudi Arabia
[d] Institut de Chimie Moléculaire de Grenoble, UAR2607 CNRS Université Grenoble Alpes, Grenoble F-38000, France
[e] KAUST Catalysis Center (KCC), Catalysis Nanomaterials and Spectroscopy, King Abdullah University of Science and Technology (KAUST), Thuwal 23955, Saudi Arabia

† Electronic supplementary information (ESI) available. See DOI: https://doi.org/10.1039/d3cy00103b

 This journal is © The Royal Society of Chemistry 2023

Open Access Article. Published on 22 March 2023. Downloaded on 2/20/2026 7:25:29 PM.
This article is licensed under a Creative Commons Attribution-NonCommercial 3.0 Unported Licence.

applied aspects (*i.e.*, enhancing aromatics yield, inhibiting coke formation). Among all the metals tested for MDA, the most interesting and promising one to replace Mo would be W, a well-known metathesis catalyst.[13,14] It is known that Mo and W differ from Cr which is also a VIB group element in terms of oxidation state stability, reactivity of oxides, ionic radii, *etc.* features.[15,16] Besides having similar chemical features to Mo (Table 1), W has certain advantages for the MDA process. One of them is its high thermal stability (Table 1). Since MoO_3-based materials may suffer from sublimation at high temperatures, the high thermal stability of WO_3 could be an advantage during high-temperature MDA reaction–regeneration cycles. Also, the interaction between Al^{3+} sites of zeolite and metal (Mo or W) is critical. In several studies, MDA-inactive extra-framework $Al_2(MoO_4)_3$ (or Anderson-type aluminum polyoxymolybdates, $Al(OH)_6Mo_6O_{18}$) species were reported on zeolites upon Mo introduction and thermal treatments.[17–19] However, in the case of W, aluminum tungstate formation could not be observed. The detailed solid-state NMR study (^{27}Al and ^{1}H–^{27}Al cross-polarization (CP) magic angle spinning (MAS) NMR) focusing on W/ZSM-5 catalysts from Feng Deng and colleagues[20] revealed that the introduction of W may lead to distortion and dealumination of the zeolite framework, but no formation of aluminum tungstate species.

On the other hand, the previous catalytic results[20–25] indubitably show that the MDA activity of W is much lower than the activity of Mo. For instance, Iglesia *et al.*[21] related the lower methane conversion and aromatics selectivity over W/H-ZSM-5 catalyst to the difficult carburization of WO_x sites *via* CH_4 compared to MoO_x counterparts. They suggested WC_x clusters as the main methane activation sites (contrary to some other studies discussed below), which they detected *in situ* after a 1 h MDA reaction at 700 °C *via* XANES. Lunsford *et al.*[24] also showed that W/H-ZSM-5 catalysts bear very low methane conversion activity at 750 °C unless they are pre-treated with CO before the reaction. In their follow-up study,[26] where they investigated various metals (V, Cr, Fe, W, and Mo) on ZSM-5 *via* XPS after CH_4 treatment at 750 °C, they could observe only sub-oxides except Mo/H-ZSM-5 for which metal-carbide (Mo_2C) was detected as well.^{13}C MAS NMR studies from Deng *et al.*[20,23] also corroborated the absence of tungsten carbide formation during MDA reaction at 627–727 °C. Although no tungsten carbide phases were detected in their case, they observed the formation of benzene, ethylene, and ethane on the catalyst. Thus, they suggested that WO_x ($x < 3$) species formed during the initial stages (*i.e.*, $WO_3 + CH_4 \rightarrow WO_x + CO + CO_2 + H_2O$) can activate methane. This was in line with the theoretical findings of Goddard *et al.*,[27] who studied various Mo, W, and Cr molecular oxide structures for methane activation *via* DFT calculations. They found that molecular WO_2 is the most active structure for the oxidative methane addition leading to methyl metal hydride (*i.e.*, H–M(O_2)–CH_3). In contrast to these, Kozlov *et al.*,[28] who applied high-resolution transmission electron microscopy on post-reacted W/ZSM-5 catalysts, found the presence of $WC_x(O_y)$ clusters inside the zeolite pores and proposed them as the main active sites for methane conversion. Besides these, Zhang and colleagues[29] studied how catalyst preparation affects the W sites and MDA activity by regulating the pH of the aqueous $(NH_4)_2WO_2$ impregnation solution. They observed the formation of $(WO_6)^{n-}$ polytungstate ions in the precursor solution prepared at low pH values (*ca.* 2–3), which was different from $(WO_4)^{2-}$ ions in the base (*i.e.*, pH 8–9) solutions. Since easier W reduction and higher MDA activity were also detected with the catalyst prepared with an acidic precursor in their experiments, they related these to the W coordination in the precursor solution. In general, although the differences and gaps between the abovementioned previous studies can be explained with catalysts (*i.e.*, preparation method, W amount, zeolite acidity), process conditions (*i.e.*, contact time, reactor structure), and inherent challenges of the characterization techniques they used, we believe that further investigations would be helpful to understand the evolution and structure of active W sites during MDA reaction.

In the present study, we studied the MDA activity of W/ZSM-5 catalysts from a different perspective. Besides comparing W catalyst to Mo one in terms of catalytic performance, we investigated how the dispersion–distribution of W sites on zeolites affects the catalytic activity *via* changing W loading and applying high-temperature reaction–regeneration cycles. In addition to a battery of advanced *ex situ* characterization techniques (*i.e.*, ^{27}Al MAS NMR, XRD-refinement, DRIFT, pyridine-IR, micro-Raman, ICP-OES, *etc.*), we attempted to shed light on the activity of tungsten catalysts *via operando* XAS and DFT-based thermodynamic analyses.

Table 1 Chemical features of molybdenum and tungsten[68,69]

	Mo	W
Group	VIB	VIB
Electron configuration[a]	[Kr]5s^{1}4d^5	[Xe]6s^{2}4f^{14}5d^4
Atomic radius (vdW)	209 pm	210 pm
Atomic mass	95.95	183.84
Maximum oxidation state	6+	6+
Ionization energy of metal	7.092 eV	7.980 eV
Ionization energy of MO_3	11.8 eV	12.5 eV
Electron affinity of metal	0.749 eV	0.816 eV
Electron affinity of MO_3	3.17 eV	3.33 eV
MO_3 melting point	795 °C	1472 °C

[a] Molybdenum is one of the exceptional elements from the diagonal rule in the periodic table.

Results and discussion

Observations on MDA performance of W/ZSM-5 catalysts

We started our investigations studying the effect of reaction temperature on catalytic performance for 2 wt% W/H-ZSM-5 (Silica/Alumina:26) catalyst (throughout the text, "*X*Metal-Z*yy*" notation was used to define the catalysts having "*X* wt% Metal" loading on H-ZSM-5 zeolite with "Silica/Alumina:*yy*"),

Open Access Article. Published on 22 March 2023. Downloaded on 2/20/2026 7:25:29 PM.
This article is licensed under a Creative Commons Attribution-NonCommercial 3.0 Unported Licence.

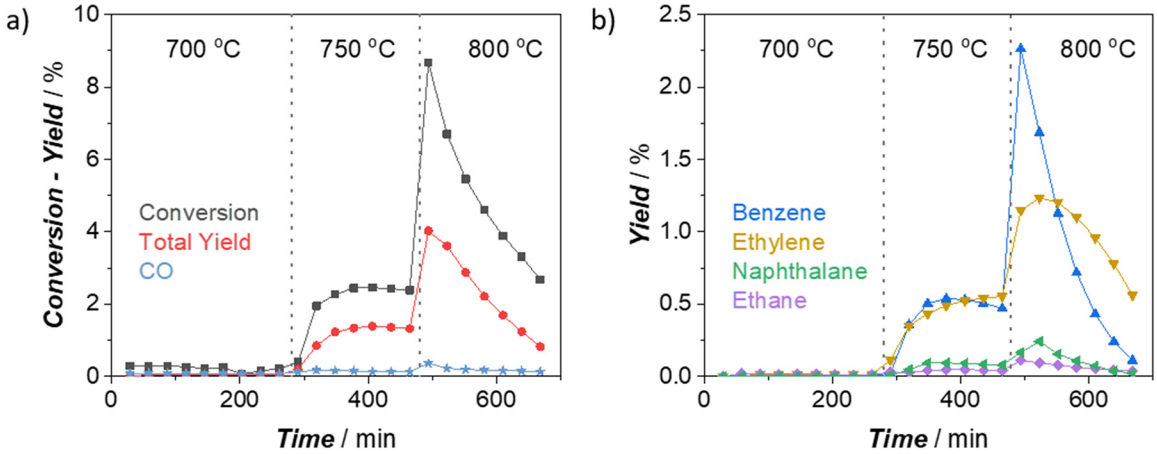

Fig. 1 Catalytic performance of 2W-Z26 (250 mg) catalyst at different temperatures under atmospheric pressure (11.8 mol% N_2 and 88.2 mol% CH_4 in the inlet, total gas flow = 17 ml min^{-1} at STP): a) CH_4 conversion, total yield (without CO and CO_2), and CO yield, b) yields of major aromatic (benzene and naphthalene) and major aliphatic (ethylene and ethane) products.

which displays a good dispersion of W on the zeolite (see the discussions below and ESI†). As depicted in Fig. 1, the MDA activity of the W catalysts at 700 °C is almost negligible, with no production of aromatics and aliphatics. This is opposite to the Mo counterpart of the catalyst we used in our previous studies.[6,17] 2Mo-Z26 shows the typical MDA activity even at 675 °C under the same reaction conditions (see section S2.1 in ESI†). These results support the previous studies[21,24,26] indicating that activation of W sites for MDA reaction is much more demanding than activating Mo. When the reaction temperature reached 750 °C, a significant amount of aromatics and aliphatics were detected in the effluent stream (Fig. 1b). However, this was different from the typical MDA activity observed over Mo/H-ZSM-5 catalysts. The benzene and ethylene yields at 750 °C were on the same level; the CH_4 conversion and total yield were not reaching peak values and quickly decaying with time, as we observed in the case of Mo catalysts. This may imply that full activation (*i.e.*, carburization) of W sites on 2W-Z26 was not achieved under this condition but partially reduced W sites seem to have the capability of attaining methane activation, as suggested by the previous studies.[20,23,26,27] When the reactor temperature reached 800 °C (Fig. 1), a typical MDA activity from the 2W-Z26 catalyst could be observed. The methane conversion and product yields reached their maximum; most importantly, benzene became the primary product, like in the case of Mo/H-ZSM-5 catalysts. This performance at 800 °C implies the activation of W sites which lead to typical MDA activity.

Furthermore, we studied how W loading affects the MDA performance at 750 and 800 °C (Fig. S3†) and examined these metal-loaded zeolites with ^{27}Al MAS NMR, PXRD, XPS, N_2 physisorption, TGA-TPO, DRIFT-IR, UV-vis DRS, and micro-Raman to understand the activity observed (see section S3 in the ESI† for detailed discussions). Catalysts having higher tungsten amounts (>2 wt%) were activated like 2Mo-Z26 catalyst at 750 °C and showed typical MDA performance (Fig. S3a–c†). This indicates that W amount and dispersion are critical parameters to initiate typical MDA activity at lower temperatures (<800 °C). Also, at both temperature levels, the overall performance (*i.e.*, methane conversion, total product yield, and H_2 production rate) was significantly enhanced, and the product yields (aliphatics and aromatics, Fig. S4a and b†) reached values comparable to 2Mo-Z26 catalyst as tungsten amount increased. However, the deactivation of the catalyst also became faster along with this enhancement in the performance related to the W amount. Similar to the previous experience[17] with 2Mo-Z26; the higher the reaction temperature becomes, the faster the deactivation gets, and the higher initial activity occurs (Fig. S3 and S4†).

To critically analyze the MDA performances of these catalysts, we also calculated the product formation rates per mole of metal atom (turnover frequency, TOF) (Fig. 2 and 3). For these calculations, we used the metal amounts found by ICP-OES analysis (Table S4†). As presented in Fig. 2, the aromatic formation rates of 2Mo-Z26 are much higher than the W-loaded catalysts at both temperatures. However, this trend changes when it comes to aliphatic formation rates (Fig. 3). Whereas 2W-Z26 has the highest aliphatics TOF values (except ethane production at the early stages of 750 °C-experiment), 2Mo-Z26 and 3W-Z26 catalysts having very close metal densities (*i.e.*, $metal_{mmoles}$ per $g_{zeolite}$, Table S4†) show similar aliphatic performance at both temperature levels. Overall, these comparisons imply that Mo is a slightly better aromatization catalyst than W despite their similar aliphatic formation rates. Also, this activity per mole of W analyses indicates that there is no linear relation between product formation rates and the amount of metal on the zeolite. This clearly reveals that active metal site formation and accessibility are different depending on the loading. Therefore, the sample characterizations should be very carefully weighed here. When the dispersion/distribution of W was investigated with micro-Raman (Fig. S16a†) and UV-vis DRS (Fig. S20 and S21†), the spectroscopic features which could be attributed to the formation of monomeric and

Open Access Article. Published on 22 March 2023. Downloaded on 2/20/2026 7:25:29 PM.
This article is licensed under a Creative Commons Attribution-NonCommercial 3.0 Unported Licence.

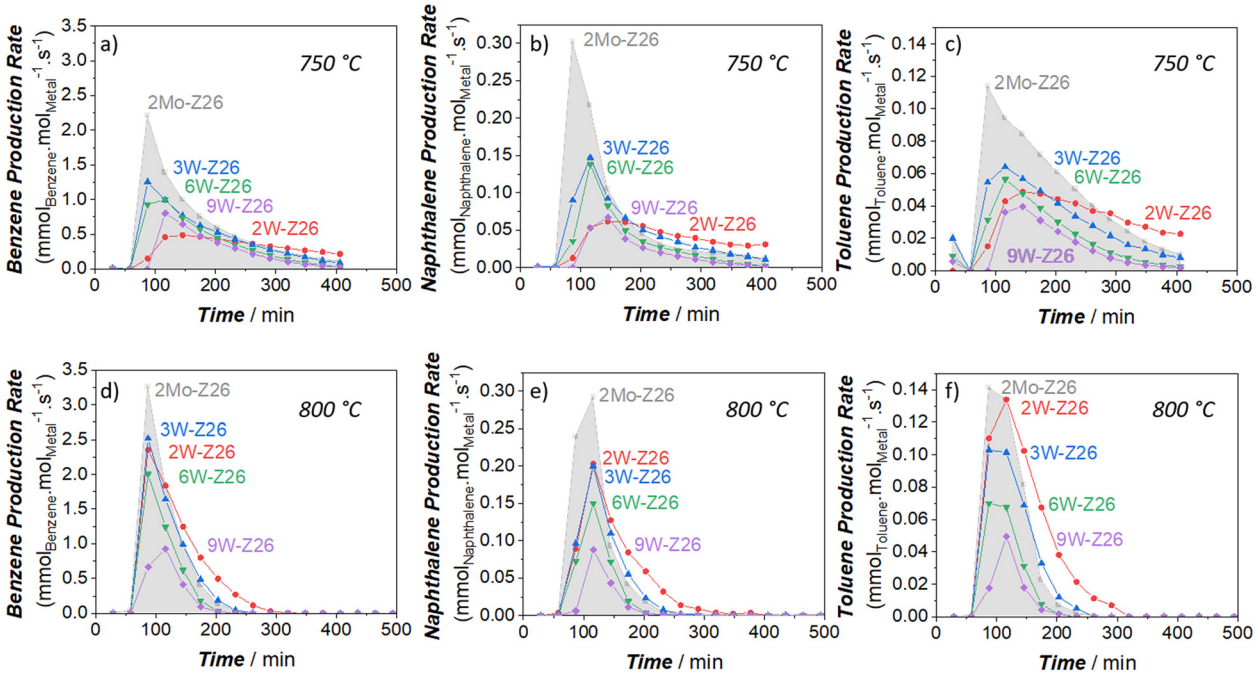

Fig. 2 Aromatic production rates (TOFs) of the prepared W and Mo catalysts (250 mg) at 750 °C (top: a–c) and 800 °C (bottom: d–f); a and d: benzene – b and e: naphthalene – c and f: toluene (11.8 mol% N_2 and 88.2 mol% CH_4 in the inlet, total gas flow = 17 ml min^{-1} at STP).

polymeric W sites in/on ZSM-5 particles were observed. However, in addition to the aforementioned W features, the crystalline WO_3 formation was observed at 9 wt% W loading. For instance, the crystalline WO_3-related vibrations (ν(O=W=O) at 811 cm^{-1}, ν(W_2O_6 & W_3O_8) at 717 cm^{-1}, and ν(O–W–O) at 272 cm^{-1}) were detected on the Raman spectrum of 9W-Z26 sample. However, these crystalline phase vibrations were broader than the bulk WO_3 vibrations, which indicates nanoparticle formation rather than larger particles.[30,31] As shown and discussed with the catalytic activity of WO_3 & ZSM-5 physical mixture catalyst (2W-Z26 Phys-Mix) in the sections below (Fig. 5f and 6f), the formation

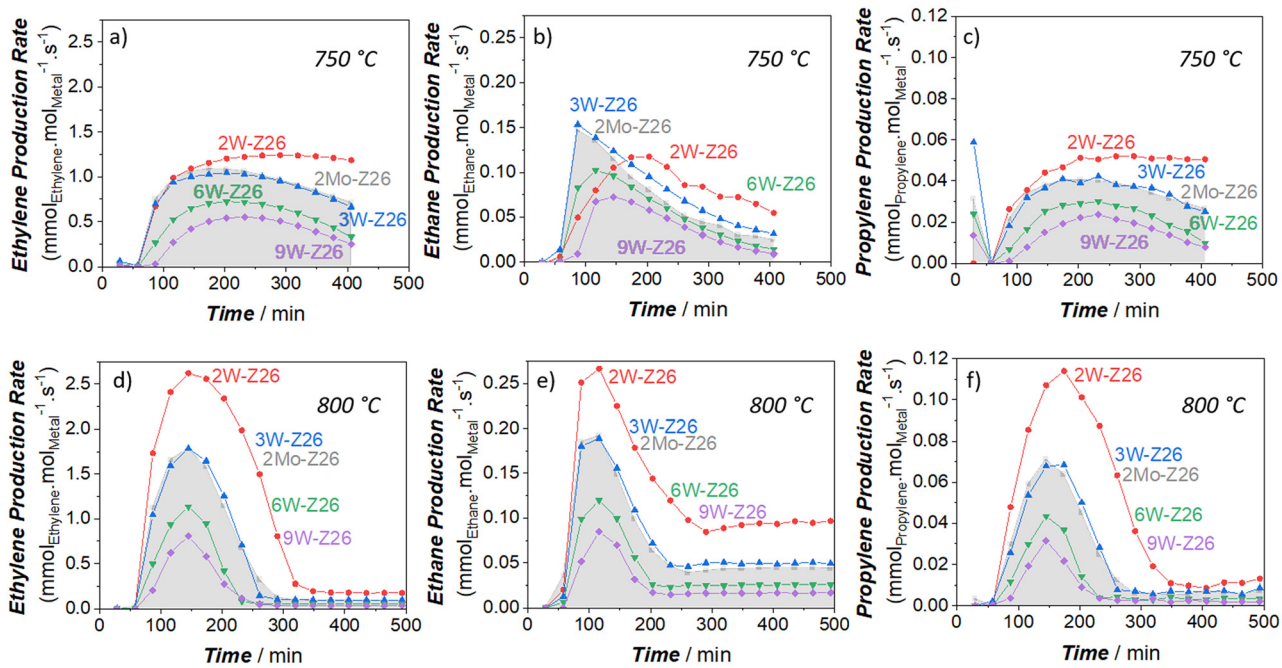

Fig. 3 Aliphatic production rates (TOFs) of the prepared W and Mo catalysts (250 mg) at 750 °C (top: a–c) and 800 °C (bottom: d–f); a and d: ethylene – b and e: ethane – c and f: propylene (11.8 mol% N_2 and 88.2 mol% CH_4 in the inlet, total gas flow = 17 ml min^{-1} at STP).

Open Access Article. Published on 22 March 2023. Downloaded on 2/20/2026 7:25:29 PM.
This article is licensed under a Creative Commons Attribution-NonCommercial 3.0 Unported Licence.

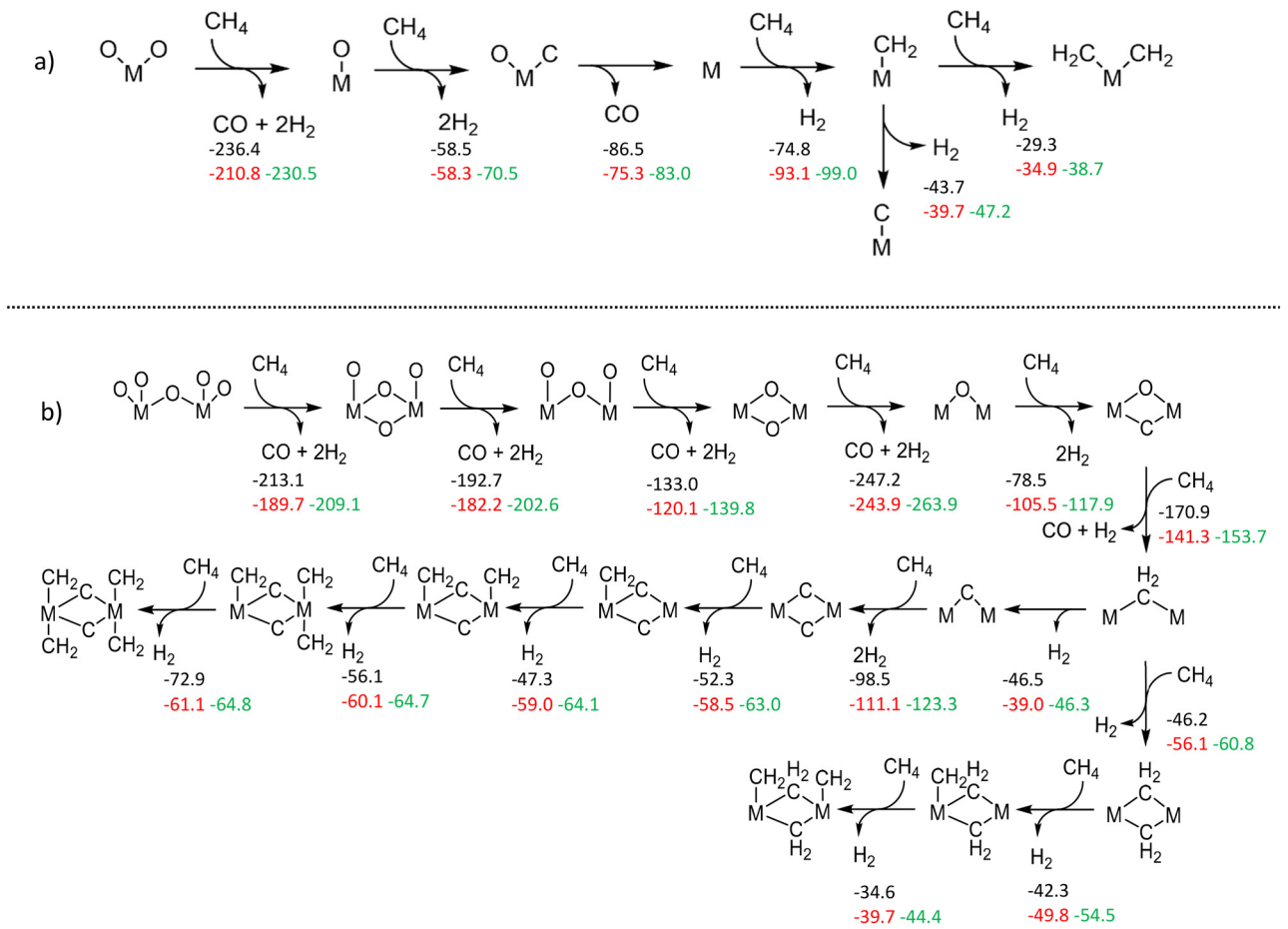

Fig. 4 Illustration of methane activation over monomeric (a) and dimeric (b) oxide species of Mo and W, with Gibbs reaction free energies provided in kcal mol^{-1} at 725 °C (Mo – black, W – red) and 800 °C (W – green) and partial pressures as P_{CO}: 10^{-15} atm, P_{H_2}: 10^{-15} atm, P_{N_2}: 0.11 atm, and P_{CH_4}: $1 - P_{CO} - P_{H_2} - P_{N_2}$ atm.

of WO_3 is very critical, because crystalline WO_3 is not a convenient precursor for active W site formation. Thus, this points out that the primary activity on the 9W-Z26 catalyst mainly resulted from well dispersed–distributed W sites in/on the zeolite particles, not from the crystalline WO_3 particles.

On the other side, we can state that 2Mo-Z26 catalyst has better metal dispersion/distribution and prevailing microporosity after Mo introduction based on our previous studies (in which we used the same catalyst)[6,17] and characterizations presented here (*vide infra* section S3 in the ESI†). However, there are also pronounced differences compared to W-samples when it comes to metal–zeolite interaction and acidity. As depicted in our previous study[17] *via* ^{27}Al MAS NMR, Mo introduction leads to aluminum molybdate formation (*i.e.*, Anderson-type aluminum polyoxymolybdates) whose tungsten-analogue was not observed in the W cases (Fig. S31†). Based on NH_3-TPD (Table 2) and pyridine-IR (Table 3), there is a sharp loss of strong acid sites on 2Mo-Z26 catalyst upon metal introduction compared to W-Z26 samples. Pyridine-IR analyses indicate that these disappeared strong acids are mostly Brønsted acid sites (BASs) since 2Mo/Z26 has a lower BAS/LAS (Brønsted acid sites/Lewis acid site, B/L) ratio compared to bare ZSM-5 and W-loaded ones (Table 3). The well-dispersion of metals, lower acid density, and lower B/L ratio of 2Mo-Z26 catalyst clearly suggest that the high aromatization activity could be linked to the active Mo sites rather than the zeolite acidity. In the case of 2W-Z26, NH_3-TPD analysis (see Table 2, Fig. S26†) revealed the loss of some acid sites upon W introduction, especially the strong ones. However, it is not to the same extent as its Mo counterpart. The loss of acidity could be explained by the anchoring of W cations on bridging oxygen sites between framework Al^{3+} and Si^{4+} atoms (see pyridine-IR data in Table 3, Fig. S28a and S29a†). However, this trend seems to be reversed at higher loadings (Table 2) since some tungsten sites provide acidity (except 9W-Z26 sample having nano-sized crystalline WO_3 particles which could block pore entrances and decrease the accessibility). It is well known that supported WO_x can act as an acid.[32–35] The amount of W, dispersion–distribution, and support type are critical factors defining this W acidity. For instance, Wachs *et al.*[33] found a correlation between site acidity and electron density

Open Access Article. Published on 22 March 2023. Downloaded on 2/20/2026 7:25:29 PM.
This article is licensed under a Creative Commons Attribution-NonCommercial 3.0 Unported Licence.

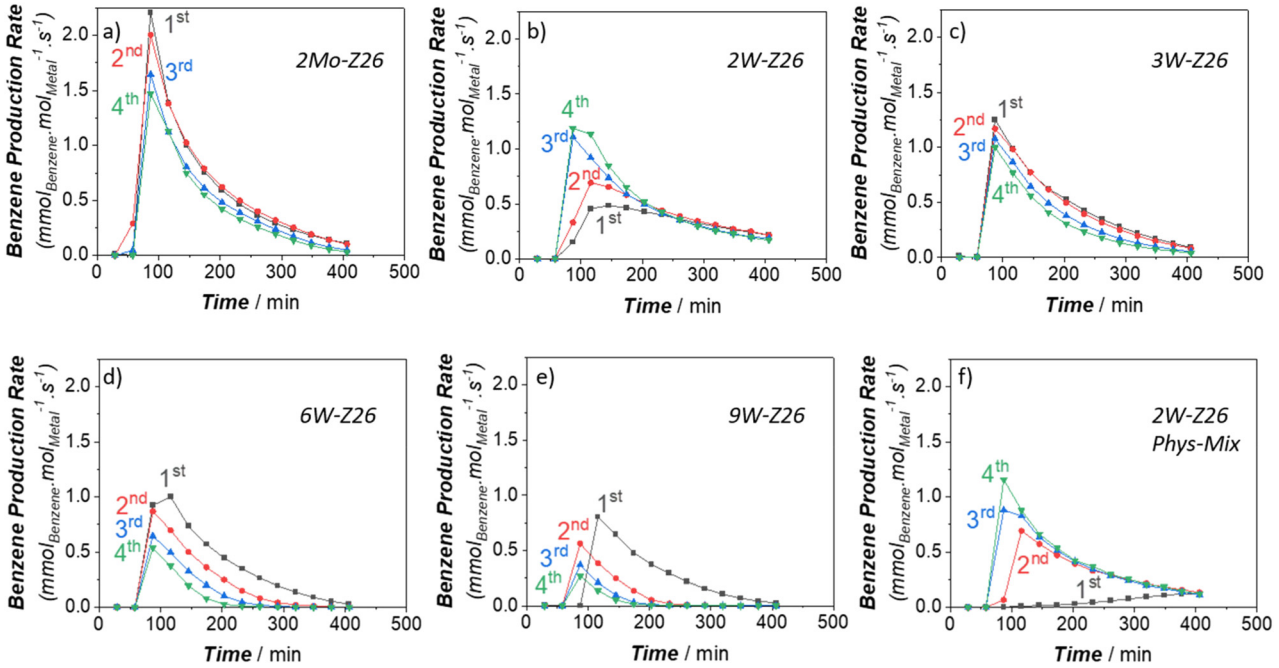

Fig. 5 Benzene production rates (TOFs) of the prepared W and Mo catalysts (250 mg) during the reaction–regeneration cycles: a) 2Mo-Z26, b) 2W-Z26, c) 3W-Z26, d) 6W-Z26, e) 9W-Z26, and f) 2W-Z26 Phys-Mix (reaction at 750 °C: 11.8 mol% N_2 and 88.2 mol% CH_4 in the inlet, total gas flow = 17 ml min^{-1} at STP – regeneration at 700 °C: dry air flow = 15 ml min^{-1} at STP).

of the bridging W–O–support bonding (*i.e.*, as support (X) cation electronegativity increases, electron density of bridging W–O–X decreases and acidity increases), when they studied supported (Al_2O_3, Nb_2O_5, TiO_2, and ZrO_2) tungsten oxide catalysts for methanol-to-dimethylether-dehydration reaction. Also, W–support interaction is closely related to the dispersion of metal sites and their reducibility. For example, previous studies[33,35] revealed that W–SiO_2 interaction is very

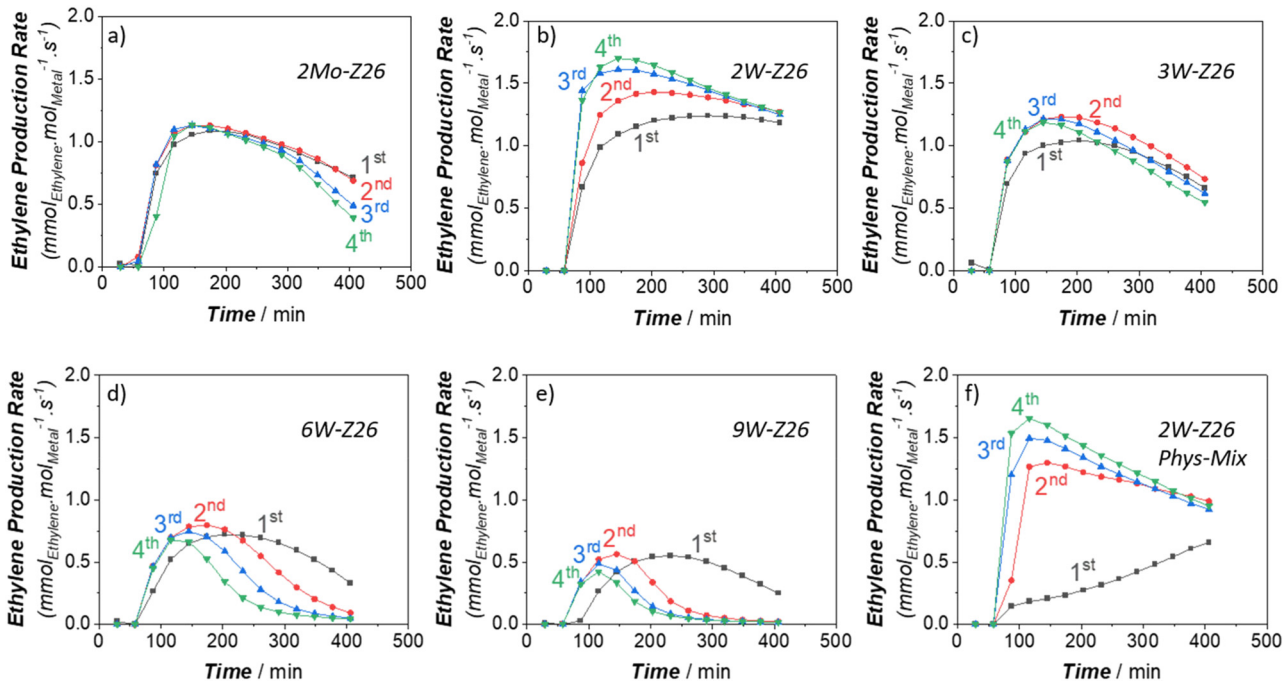

Fig. 6 Ethylene production rates (TOFs) of the prepared W and Mo catalysts (250 mg) during the reaction–regeneration cycles: a) 2Mo-Z26, b) 2W-Z26, c) 3W-Z26, d) 6W-Z26, e) 9W-Z26, and f) 2W-Z26 Phys-Mix (reaction at 750 °C: 11.8 mol% N_2 and 88.2 mol% CH_4 in the inlet, total gas flow = 17 ml min^{-1} at STP – regeneration at 700 °C: dry air flow = 15 ml min^{-1} at STP).

Open Access Article. Published on 22 March 2023. Downloaded on 2/20/2026 7:25:29 PM.
This article is licensed under a Creative Commons Attribution-NonCommercial 3.0 Unported Licence.

Table 2 Ammonia TPD analyses of pristine ZSM-5 and metal-loaded ZSM-5 catalysts, see Fig. S26† for profiles

Samples	Peak position (°C)		Amount (μmol g^{-1} at STP)		
	Weak acid	Strong acid	Weak acid	Strong acid	Total acid
Z26	201	361	282	427	709
2W-Z26	203	346	290	321	611
3W-Z26	209	361	316	353	669
6W-Z26	205	338	337	360	697
9W-Z26	205	320	338	282	620
2Mo-Z26	205	342	302	260	562

weak compared to W–Al_2O_3, and this could lead to bigger particles (*i.e.*, polytungstates and aggregated crystalline WO_3) compared to highly dispersed species (*i.e.*, isolated tetrahedral) on alumina supports. Moreover, reducing tungsten sites on alumina were found more demanding than reducing tungsten sites on silica support *via* H_2.[35]

The MDA activity differences observed between 2W-Z26 and other W loaded catalysts at 750 °C could be explained through considering these. Apparently, there is a high probability of forming WO_x sites attached to silanol groups and located on the external surface at higher loadings (>2 wt%). So, these W-sites attached to "silica phase" of zeolite could be easily activated/reduced in comparison to other tungsten sites attached to the BASs inside the pores. Eventually, this results in the activity differences (typical MDA *vs.* non-typical MDA) between 2W-Z26 and higher W-loaded samples at 750 °C. Similar examples showing a correlation between overall activity and W–support interaction can also be found in the literature[36] (*vide infra* section S3 in the ESI†).

Beyond these, the pyridine-IR analyses performed to investigate the acid sites of fresh Z26, 2W-Z26, and 6W-Z26 depict that the number of BASs sharply decreases upon W introduction to zeolite compared to the decrease in the number of LASs (at 150 °C – after removing physisorbed pyridine). This indicates that W cations replace protons of some BASs. However, 6W-Z26 has slightly higher BASs than 2W-Z26 at 150 °C, which could mean there are more polymeric W sites at 6 wt% loading and results in more free zeolite BASs. When we further treated the samples at 350 °C and forced some pyridine to desorb, it was noticed that 2W-Z26 and 6W-26 have a similar number of BASs but 6W-Z26 has a higher amount of LASs. These LASs resulted from W-sites may explain the higher catalytic activity of 6W-Z26 at 750 °C. It is known that Lewis acid–base pairs can activate C–H bonds heterolytically:[37] the electron-deficient/undercoordinated metal site (Lewis acid) can polarize the C–H bond and form σ-bond with CH_3 moieties while pair basic site (*i.e.*, neighbouring basic oxygen center) accepts a proton. Also, while one-oxidation state (W^{6+}) was observed at 2 wt% loading, W^{5+} features were also identified to a small extent at 6 wt% loading on the XPS spectra (Fig. S30†) collected for fresh samples. The latter could imply that the formation of defective W sites becomes more probable at higher loadings. These defects could ease the activation of W sites (*vide infra* section S3 in the ESI†).

Understanding the MDA activity through DFT-based thermodynamic calculations: Mo *vs.* W

To gauge the reduction and stability of W species, we benefited from DFT-based calculations as we did in our previous publication.[17] First of all, monomeric and dimeric W structures anchored on ZSM-5 were built and optimized (Fig. S54†). Then, we performed thermodynamic analysis for reduction-*via*-methane reactions of respective W and Mo states under a gas phase composition similar to the experimental one (for more details see section S5†).

The thermodynamic analyses provided in Fig. 4 reveal that the different exergonic and endogenic steps for Mo structures are also exergonic and endogenic for the corresponding W models. In other words, they have similar trends (also see Fig. S55, S56, S58–S63 in the ESI†). However, when we compare the extent of exergonicity, we see that Mo species (both dimeric and monomeric) are significantly more prone to get reduced during the initial oxygen removal steps compared to W. This difference between the two metals could explain why it is much more demanding to activate W/ZSM-5 catalysts and attain typical MDA activity. Also, it is noteworthy that the reduction of dimeric structures is thermodynamically more spontaneous than monomeric ones. Since the formation of dimeric/polymeric structures is more possible at higher W loadings (>2 wt%), this finding can explain the observation of typical MDA activity for higher W loadings at 750 °C.

Another notable difference between Mo and W structures is the addition of carbenes (:CH_2) to reduced/carbidic structures (Fig. 4). In the case of W structures, the reaction steps leading to the formation of carbene moieties are mostly

Table 3 Pyridine-IR data (BAS: Brønsted acid sites, LAS: Lewis acid site, B/L: BAS/LAS) obtained for fresh samples (Z26, 2W-Z26, 6W-Z26, and 2Mo-Z26) upon 150 and 350 °C treatments. For the spectra, please see Fig. S28a and S29a†

Samples Fresh	150 °C				350 °C			
	BAS (μmol g^{-1})	LAS (μmol g^{-1})	Total (μmol g^{-1})	B/L	BAS (μmol g^{-1})	LAS (μmol g^{-1})	Total (μmol g^{-1})	B/L
Z26	409.2	264.6	**673.8**	**1.55**	251.9	95.7	**347.6**	**2.63**
2W-Z26	314.8	209.6	**524.4**	**1.50**	203.0	81.7	**284.7**	**2.49**
6W-Z26	334.6	202.6	**537.2**	**1.65**	202.5	97.0	**299.5**	**2.09**
2Mo-Z26	199.5	230.8	**430.3**	**0.86**	104.6	79.7	**184.4**	**1.31**

Open Access Article. Published on 22 March 2023. Downloaded on 2/20/2026 7:25:29 PM.
This article is licensed under a Creative Commons Attribution-NonCommercial 3.0 Unported Licence.

more exergonic than Mo. This relative thermodynamic difference could help us in understanding the activity differences between Mo and W catalysts that we observed. Considering the arguments on carbenes which are considered as key intermediates for coupling and further oligomerization steps,[38] we studied the thermodynamic feasibility of ethylene formation through the dimeric and monomeric structures in this study (*vide infra* Fig. S57†). It was found that carbene-dimerization-to-ethylene is relatively more thermodynamically favorable on Mo than on W. This could explain the activity difference between the two metals.

In general, our computational analysis corroborates our experimental findings, but one should remember the clusters we studied are simplified models. The real sites on zeolites are much more complex and dynamic, as we discussed throughout this study.

High temperature reaction–regeneration cycles of W/ZSM-5 catalysts

In the next phase of this study, to gain more in-depth insight into W activity, we applied high-temperature reaction–regeneration cycles on all catalysts mentioned in the previous sections (*i.e.*, reaction at 750 °C–regeneration at 700 °C). This type of cyclic MDA performance evaluations for W-loaded catalysts was never performed before in previous studies. Here we brought benzene and ethylene TOFs (Fig. 5 and 6) to the fore since they are the major aromatic and aliphatic products, respectively (see Fig. S5–S9 in ESI† for other products). It is clear that the performance of 2Mo-Z26 catalysts deteriorated after each regeneration step (Fig. 5a and 6a), especially aromatics formation capability. However, in the case of its W counterpart (2W-Z26), the performance – particularly initial activity – was getting enhanced after each cycle (Fig. 5b and 6b); surprisingly, all production rates were significantly higher. One may relate the difference between these two catalysts to possible loss (*i.e.*, sublimation) of Mo, but when we checked both catalysts after 4 regeneration cycles with ICP-OES, loss of metals was not detected (Table S4†). On the other hand, provocatively, as the W amount increases (>2 wt%), the enhancement tendency is no longer there. In contrast, the product formation rates (especially benzene) decreased, and much quicker deactivation was observed (Fig. 5c–e and 6c–e). So, this implies that 2W-Z26 catalyst, which was not fully activated in the first reaction run like the others (see the previous sections), experienced some structural changes leading to improved activity while others were degrading. To confirm that this enhancement tendency is dependent on W loading, we prepared another 2W-Z26 catalyst by simply mixing bulk WO_3 and H-ZSM-5 physically (2W-Z26 Phys-Mix). The prepared catalyst showed almost negligible activity in the first run (Fig. 5f and 6f), especially for aromatics. This demonstrates that bulk WO_3 is not a convenient precursor for active W site formation. On the other hand, 2W-Z26 Phys-Mix behaved like its equivalent after the regeneration steps; showed enhanced activity in a similar trend. This indicates there should be an optimal W loading range for the enhancement behavior. Furthermore, we investigated the effect of the zeolite's silica/alumina ratio (SAR) since it affects the distribution–dispersion of metal sites. As shown in Fig. S10a and b,† we applied the same reaction–regeneration cycles to the 2W-Z371 catalyst, which has higher SAR (371), and we did not observe a considerable enhancement in the production rates compared to 2W-Z26 catalyst. However, it also did not degrade either. So, it can be interpreted the aluminum content of the zeolite also plays a crucial role during the reaction–regeneration cycles.

Besides these, one may also question the effect of regeneration during all these investigations. As we mentioned before, the regeneration process occurs at 700 °C under continuous air-flow. However, when we prepared the fresh catalysts, they were calcined at 550 °C in a muffle furnace (*i.e.*, static conditions). To check how the regeneration conditions affect the fresh 2W-Z26 catalyst, we decided to pre-calcine it at 700 °C under continuous flow for 7 days prior to the reaction test at 750 °C. The obtained performance (Fig. S10c and d†) showed no enhancement in the activity; higher calcination temperature under dynamic conditions is not helpful in re-distributing/re-dispersing the W sites. To get the enhancement, a spent version of the catalyst (*i.e.*, reduced W sites and coke deposition) is required. Meanwhile, we also looked into the effects of reaction–regeneration cycle parameters (*i.e.*, temperature level, experimental duration, number of cycles). The cyclic pathways followed during the catalysis experiments are depicted in the ESI† (see section S2.5). In one of these pathways, when we regenerated the 2W-Z26 catalysts at 700 °C for 16 h upon the first reaction test at 750 °C, we noticed faster aging for the second reaction run, which led to the highest activity we observed in the original pathway (Fig. S13c and f†). Also, we realized this enhancement in the activity has a limit; the activity started declining after a few more cycles.

Effects of reaction–regeneration cycles on catalysts

The first thing we noticed on all samples after four regeneration cycles, the sample color was becoming light brownish (Fig. S17†). Initially, we thought that this color change might be related to tungsten sites (*i.e.*, partially reduced W oxides[39]), but we observed the same color change in the case of 2Mo-Z26 catalyst and bare ZSM-5 when we applied the same reaction–regeneration cycles. Also, XPS measurements on 2W-Z26 and 6W-Z26 confirm that oxidation states of W sites are recoverable even after 4 regeneration cycles (Fig. S30†). While investigating these samples with micro-Raman, we noticed that these brownish parts were localized, and they were very sensitive to laser irradiation under air (see Fig. S18†). This brought to mind that they might be coke species, although we didn't observe any coke-related mass loss when we performed TPO with regenerated samples (Fig. S24†). However, when we further

Open Access Article. Published on 22 March 2023. Downloaded on 2/20/2026 7:25:29 PM.
This article is licensed under a Creative Commons Attribution-NonCommercial 3.0 Unported Licence.

analyzed these regenerated samples with UV-vis DRS (Fig. S21b†), we confirmed the presence of some persistent coke-type species (*i.e.*, poly-aromatics, alkylated-naphthalenes)[40,41] even after the high-temperature regeneration of spent catalysts.

Moreover, the N_2 physisorption analysis (Tables S1–S3, and Fig. S14 and S15†) demonstrates that after four reaction–regeneration cycles, there is a noticeable decrease in the surface area and the pore volume for all samples (especially the ones having higher W loading). This degradation in the porous structure can be explained by the trapped carbon species – which we discussed above – and the deformations in the catalyst structure. When we analyzed 2W-Z26 and 6W-Z26 samples *via* solid-state ^{27}Al MAS NMR to probe the local atomic environment related to Al, significant changes were noticed after the reaction–regeneration cycles (^{27}Al and ^{29}Si MAS NMR: Fig. S31a and b,† respectively). In the regenerated samples, the dealumination of the zeolite framework was observed, showing broad distribution ^{27}Al resonances with penta-coordinated ^{27}Al species at *ca.* 30 ppm. We could also observe the formation of extra framework Al species (EFAl) after regeneration cycles, in line with the DRIFT results (Fig. S23†). Meanwhile, neither on fresh nor on regenerated samples, any ^{27}Al resonances related to aluminum tungstate species were not observed. This corroborated the absence of these species in W-incorporated ZSM-5 catalysts reported in earlier studies.[20,28] Besides this, we further identified the formation of defects *via* UV-vis DRS for all samples – including 2Mo-Z26 – as well (see Fig. S22† caption for the details). Furthermore, we investigated the crystallographic features in all these samples *via* PXRD analysis (Fig. S32 and Table S5†). The crystallinity, as well as the coherent domain size of the regenerated samples, does not change much compared to their fresh counterparts. To support this observation, there are many examples showing that after high-temperature steam treatment – the crystallinity of zeolites does not degrade despite the dealumination of framework and formation of defects.[42–45] Moreover, the event of dealumination after the catalytic cycle can be evidenced from PXRD data, comparing the relative intensities of (011) or (200) and (501) diffraction peaks, $I^{(011)}/I^{(501)}$ or $I^{(200)}/I^{(501)}$, (see Fig. S33–S35, Table S5† and its caption for further details).[46]

On the other hand, the *ex situ* characterizations performed to unveil the changes in tungsten and molybdenum sites are delicate and complicated. To compare the fresh and regenerated samples (4 cycles), first, we performed micro-Raman measurements under ambient conditions (Fig. S16 and S19†). We noticed W-related Raman shifts on fresh samples (*i.e.*, 973 cm^{-1}: ν(O═W═O) from surface WO_4 species, 828 cm^{-1}: ν(W–O–W)) disappeared after several regenerations (except the bulk WO_3 vibrations on 9W-Z26 catalyst). Instead of these, we observe a vibration band at *ca.* 1015 cm^{-1} which could be assigned to mono W═O stretching of surface WO_5/WO_6 polytungstates and WO_5 monotungstates species.[47] A similar situation was also observed on 2Mo-Z26 catalyst after regeneration cycles (Fig. S19†). In the case of UV-vis spectra, it is complicated to identify and analyze the W and Mo-related absorptions since zeolite defects and coke-related absorptions also exist (Fig. S20 and S21†). The absorptions at *ca.* 209 and *ca.* 260 nm could be attributed to mono- and polytungstates different than the ones observed on fresh catalysts. Beyond any doubt, the dispersion and distribution of metal on regenerated samples change sharply compared to the sites on fresh catalysts. At the same time, it is clear that coke combustion during the regeneration is changing the zeolite structure (*i.e.*, defects, dealumination), and this affects the metal dispersion–distribution.

To gain more insight into the catalyst during these regeneration cycles, we performed acidity analysis (pyridine-IR) on four times regenerated Z26, 2W-Z26, 6W-Z26 and 2Mo-Z26 samples. First of all, there was a sharp decrease in the total number of acid sites for all four samples compared to their fresh versions (Table 4). Considering the values upon treatment at 150 °C, we could state that the decrease in BASs is much more significant while the number of LASs increases slightly in the case of ZSM-5 and 2W-Z26. This result clearly suggests that we are forming defects (*i.e.*, EFAl) that induce Lewis acidity. It is also perceptible that 2W-Z26 catalyst has the highest BAS/LAS ratio compared to the other three. This may explain the increasing trend in 2W-Z26's activity during the high-temperature reaction–regeneration cycles. While re-dispersing and re-distributing tungstens, preserving a certain amount of BASs that can contribute to aromatization and hydrocarbon-pool mechanism might be very critical. On the other hand, four times regenerated 2Mo-Z26 catalyst has the lowest B/L ratio – like we observed in the case of fresh catalysts. Again, this corroborates the aromatization capability of active Mo sites over active W sites.

Besides these, we investigated the spent 2W-Z26, 6W-Z26 and 2Mo-Z26 catalysts after the first and third reaction steps *via* TPO and N_2 physisorption techniques (Table 5, Fig. S14b and S25†). Based on the data obtained *via* TPO, 6W-Z26 catalysts have a slightly higher amount of coke compared to 2W-Z26 and 2Mo-Z26 after both steps, but the difference is not so high. Also, the coke amount decreases as these catalysts were further regenerated and tested. This trend could be attributed to the BAS degradation and re-dispersion/re-distribution of tungsten and molybdenum sites. Although the thermal gravimetric analysis does not show sharp differences between the three samples, N_2 physisorption analyses set forth the differences between them during the deactivation. Despite having close coke amounts after both reaction steps, 2W-Z26 and 2Mo-Z26 spent samples have still considerable free porosity whereas the pores of 6W-Z26 are almost fully blocked. This is indicating that the coke distribution behavior in/on zeolite particles differs between the samples. From the previous studies with Mo/ZSM-5 catalysts, it is well-known that Mo species inside the pores are carburized by detaching from the zeolite pores and forming clusters on the outer surface that leads to coke accumulation and sintering of the active molybdenum

Open Access Article. Published on 22 March 2023. Downloaded on 2/20/2026 7:25:29 PM.
This article is licensed under a Creative Commons Attribution-NonCommercial 3.0 Unported Licence.

Table 4 Pyridine-IR data (BAS: Brønsted acid sites, LAS: Lewis acid site, B/L: BAS/LAS) obtained for four times regenerated samples (Z26, 2W-Z26, 6W-Z26, and 2Mo-Z26) upon 150 and 350 °C treatments. For the spectra, please see Fig. S28b and S29b†

Samples 4× regenerated	150 °C				350 °C			
	BAS (μmol g^{-1})	LAS (μmol g^{-1})	Total (μmol g^{-1})	B/L	BAS (μmol g^{-1})	LAS (μmol g^{-1})	Total (μmol g^{-1})	B/L
Z26	109.2	274.3	**383.5**	**0.40**	36.2	70.4	**106.6**	**0.51**
2W-Z26	128.0	210.4	**338.4**	**0.61**	31.9	50.9	**82.8**	**0.63**
6W-Z26	96.7	184.8	**281.5**	**0.53**	20.6	38.0	**58.6**	**0.54**
2Mo-Z26	96.7	197.6	**294.3**	**0.49**	26.3	78.5	**104.9**	**0.34**

carbide sites.[48] Eventually, the same behavior can be expected for the tungsten version of the catalyst. And this can explain why the porous structure of 6W-Z26 was heavily blocked compared to 2W-Z26 since it has a higher amount of W. In the TPO profile of 6W-Z26 (Fig. S25b†), the oxidation of big WC_x clusters could be seen around 510 °C. The unexpected result here is that while 2W-Z26 catalyst gives better performance and 6W-Z26 gets worse after each regeneration cycle, both have decreasing coke content trends. These might be attributed to the loss of BASs (Table 4) which could lead to coking-related deactivation in zeolite catalysis and/or different kinds of active tungsten sites on these two catalysts (which we discussed in the next section).

Operando X-ray absorption spectroscopy: active tungsten-species

We performed *operando* X-ray absorption spectroscopy (XAS) analysis to shed light on the W sites and how they behave during the reaction–regeneration cycles. The characterization of catalysts under high-temperature reaction/regeneration conditions was performed using a dedicated cell designed as a plug-flow reactor for *operando* XAS at the Neel Institute in Grenoble, France (see the further details in section S1.4 and S4†).[49] In order to identify the nature of active W species of the 2W-Z26 and 6W-Z26 catalysts during MDA reaction, W L_3-edge EXAFS spectra of the fresh catalysts were collected during the different stages of reaction–regeneration cycles with the same space velocity. Based on the effluent gas analysis performed with the mass spectrometer (Fig. S45†), we confirmed the reproducibility of the catalytic tests obtained with PID fixed-bed reactor. Also, we noticed changes in the initial activation-induction period during the *operando* experiments (see Fig. S48† for details).

Fig. 7 shows the W L_3-edge XANES spectra of the two 2W-Z26 and 6W-Z26 fresh catalysts and reference samples including tungsten trioxide WO_3, sodium monotungstate Na_2WO_4 (aq) obtained from the Solid Spectroscopy Hosting Architecture of Databases and Expertise (SSHADE),[50] and ammonium metatungstate $(NH_4)_6H_2W_{12}O_{40}$. All the spectra contain a white line at 10 213.5 eV, which is characteristic of tungsten oxide W(VI) species.[51,52] However, each sample has a differently shaped white line, which can be attributed, according to Yamazoe *et al.*,[53] to the difference in structure. For example, the WO_3 reference sample having a white line of lower intensity, is known to have a distorted octahedral $[WO_6]$ symmetry structure.[53–55] In contrast, the increase in the intensity of the white line for the monotungstate reference sample WO_4^{2-} (aq) is related to the presence of W atoms in a tetrahedral environment $[WO_4]$.[53–56] For both 2W-Z26 and 6W-Z26 fresh catalysts, their XANES spectra is similar to that of ammonium metatungstate $(NH_4)_6H_2W_{12}O_{40}$, which indicates that the catalysts are deposited as polytungstate species on the support after impregnation. This is consistent with the white line intensity of both catalysts located between those of the WO_3 and WO_4^{2-} (aq) references, thus confirming the presence of mixed W(VI) tetrahedral and octahedral clusters. The higher intensity of the white line of

Table 5 Nitrogen physisorption analyses of fresh, spent, and four-times regenerated samples with TGA analyses for the spent samples

Samples	S_{BET} (m^2 g^{-1})	$S_{meso/ext}$ [a] (m^2 g^{-1})	S_{micro} [b] (m^2 g^{-1})	V_{total} [c] (ml g^{-1})	V_{micro} [b] (ml g^{-1})	Coke % [d] ($mass_{coke}$ per $mass_{catalyst}$)
2W-Z26 fresh	397	104	293	0.23	0.11	—
2W-Z26 4× regenerated	372	79	293	0.22	0.11	—
2W-Z26 1× reaction	129	35	94	0.09	0.04	20.3%
2W-Z26 3× reaction	221	40	181	0.13	0.07	17.0%
6W-Z26 fresh	372	100	272	0.21	0.11	—
6W-Z26 4× regenerated	321	81	240	0.20	0.09	—
6W-Z26 1× reaction	31	22	9	0.04	0.00	22.3%
6W-Z26 3× reaction	30	21	9	0.04	0.00	19.0%
2Mo-Z26 fresh	384	98	286	0.22	0.11	—
2Mo-Z26 4× regenerated	352	89	264	0.21	0.10	—
2Mo-Z26 1× reaction	142	32	110	0.09	0.04	20.1%
2Mo-Z26 3× reaction	162	130	32	0.10	0.05	16.9%

[a] $S_{meso/ext} = S_{BET} - S_{micro}$. [b] From N_2 adsorption isotherm using the *t*-plot method. [c] Single point adsorption total pore volume at $p/p^o = 0.95$. [d] Calculated from TG-TPO data.

Open Access Article. Published on 22 March 2023. Downloaded on 2/20/2026 7:25:29 PM.
This article is licensed under a Creative Commons Attribution-NonCommercial 3.0 Unported Licence.

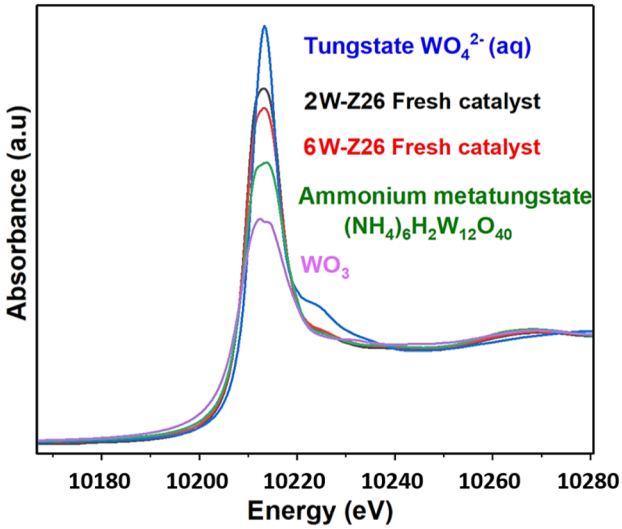

Fig. 7 W L_3-edge XANES spectra of the 2W-Z26 and 6W-Z26 fresh catalysts compared with tungsten trioxide (WO_3), ammonium metatungstate $(NH_4)_6H_2W_{12}O_{40}$ and sodium monotungstate Na_2WO_4 (aq) reference compounds.

the 2W catalyst compared to that of the 6W may be due to a better dispersion of the particles after impregnation, as shown in the high-resolution HAADF-STEM images of the two fresh catalysts (Fig. S36 and S37†).

In order to understand the structural evolution of the W catalysts during the different reaction/regeneration cycles, we compared their XANES spectra obtained *operando* to those of the fresh catalysts and the Na_2WO_4 (aq) reference. Fig. 8 shows the W L_3-edge XANES spectra of the 2W-Z26 and 6W-Z26 catalysts during the reaction cycles (under CH_4/He, 750 °C) and after regeneration with air at 700 °C. In both cases, a clear evolution of the fresh 2W and 6W catalysts is observed during the reaction, with the same behavior obtained during the three cycles. Indeed, the appearance of a shoulder at 10 224 eV is revealed. This type of oscillation was only observed (greatly) in the case of WO_4^{2-} monotungstate reference (Fig. 8),[51,57] and may then indicate the dispersion of the W species (polytungstates) initially present in monotungstates species during the reaction. This can be confirmed by the aberration-corrected HAADF-STEM images (Fig. S36 and S37†), showing the presence of highly dispersed single tungsten atoms, corresponding to surface monotungstate species, and polytungstates clusters, as previously observed in literature.[58–60] Furthermore, the absorption edge of the XANES spectra shifts to lower energy during the reaction for both 2W-Z26 and 6W-Z26 catalysts (Fig. 8), which can be attributed to the chemical shift effect. Generally, the shift in edge position can be attributed to a change in the oxidation state of an element.[61] An overall shift of the XANES spectra to higher energies is observed as the oxidation state increases. Indeed, when the global charge of the atom is more positive at higher degrees of oxidation, more energy is required to excite an electron out of an orbital. Conversely, the XANES spectrum shifts to lower energy when the metal element is more reduced, *i.e.* when there is less positive charge on the metal. Therefore, to get an idea of the oxidation state of tungsten in the two catalysts during the MDA reaction, a linear relationship between the W L_3-edge energy and the W oxidation state was established, using the W references (Fig. 9). The W L_3-edge absorption energies of the reference materials were 10 209.7 eV for W foil (W^0), 10 212.1 eV for WO_2 (W^{4+}), and 10 213.5 eV for WO_3 (W^{6+}). The absorption edges of the two catalysts are very close to those of WO_3, indicating that both catalysts have a W^{6+} oxidation state before the MDA reaction. During the reaction, the absorption edges of the 2W and 6W catalysts were lower than those of the fresh counterparts and were particularly localized between those of the W foil and WO_2 references. This is an indication that both catalysts exhibit a reduction in their oxidation state during the reaction, and that the W

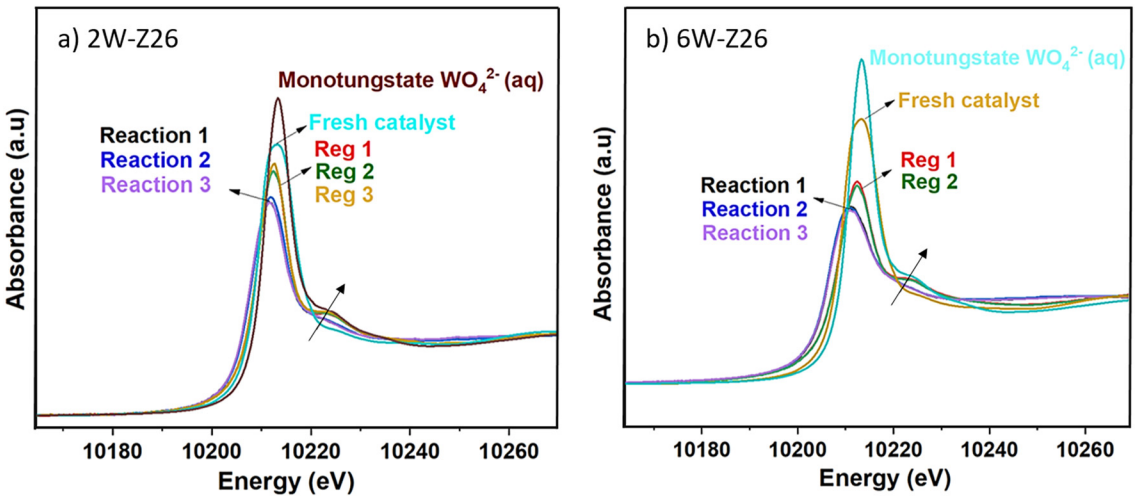

Fig. 8 W L_3-edge XANES spectra of a) 2W-Z26 and b) 6W-Z26 catalysts before and during different reaction/regeneration cycles. The experimental spectra of the two catalysts are compared to the sodium monotungstate Na_2WO_4 (aq) reference spectra.

Open Access Article. Published on 22 March 2023. Downloaded on 2/20/2026 7:25:29 PM.
This article is licensed under a Creative Commons Attribution-NonCommercial 3.0 Unported Licence.

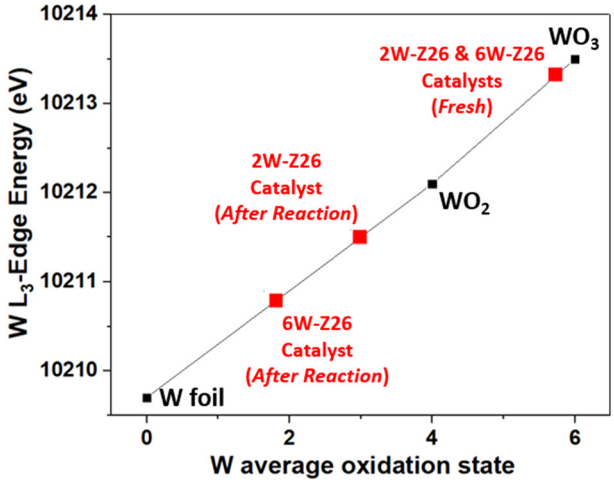

Fig. 9 Average oxidation states of tungsten obtained from W L3-edge XANES for the references (W foil, WO_2, and WO_3) and the 2W-Z26 and 6W-Z26 catalysts before reaction (fresh catalysts) and during MDA reaction.

absorber shifts from a W^{6+} oxidation state to a mixture of oxidation states, namely between W^{2+} and W^{4+}. However, the overall reduction of W sites in the case of 6W-Z26 was much sharper compared to the ones in 2W-Z26 catalyst during the reaction, which may indicate the difference in the active W site structures and oxidation states.

After regeneration in air at 700 °C (Fig. 8), we observe a remarkable increase of the shoulder present at 10 224 eV. Indeed, the XANES spectra of the two catalysts after regeneration become very similar to that of the Na_2WO_4 (aq) reference containing monotungstate WO_4^{2-} species. This indicates that the state of the catalyst obtained after regeneration is different from its initial state just before the first reaction, with the presence of monotungstates species better dispersed on the support than those of polytungstates present in the 2W and 6W fresh catalysts. This well dispersed–distributed W sites after regeneration can explain the better catalytic activity of the 2W-Z26 catalyst during the second reaction cycle. However, what is surprising is that the 6W-Z26 catalyst shows a lower catalytic activity during the second reaction cycle, probably due to a difference in structure, which cannot be distinguished in XANES analysis.

To have a clearer idea of the structure of the catalysts and the nature of the tungsten species present during the reaction, as well as that formed after regeneration, the radial distribution functions of the EXAFS spectra (FT-EXAFS) of each catalyst during the different reaction/regeneration cycles are showed in Fig. 10 (the corresponding k^2-weighted EXAFS spectra are shown in Fig. S49 in ESI†). For a more comprehensive comparison, the experimental FT-EXAFS spectra and their corresponding Cauchy wavelet transforms are compared to those of known reference spectra WO_3, Na_2WO_4 (aq), ammonium meta tungstate ($(NH_4)_6H_2W_{12}O_{40}$) and WC obtained at room temperature (see Fig. S50–S53 in ESI†). Both catalysts exhibit one large feature around 1.7 Å during MDA reaction and regeneration under air at 700 °C. This peak corresponds to the first W-coordination shell in which the anion of the oxygen atoms surrounds the central atom.[62,63] Peaks less than 1 Å generally do not correspond to actual coordination spheres and may appear from atomic XAFS and/or multi-electron excitations.[64] The difference in peak intensity at 1.7 Å between the reaction and the regeneration cycles is due to a modification of the structure of the W species. In general, the disordered octahedral structure of the W(VI) species results in octahedral W–O shells showing much lower intensities than ordered tetrahedral tungstates. Obtaining a higher intensity during regeneration can then explain the formation of well-dispersed monotungstates WO_4^{2-} species, which is consistent with XANES analyses (Fig. 8). On the other hand, the decrease in intensity during the reaction indicates that a mixture of W(VI) tetrahedral and octahedral clusters is formed (mono/polytungstates), and some sites are reduced. The noticeable

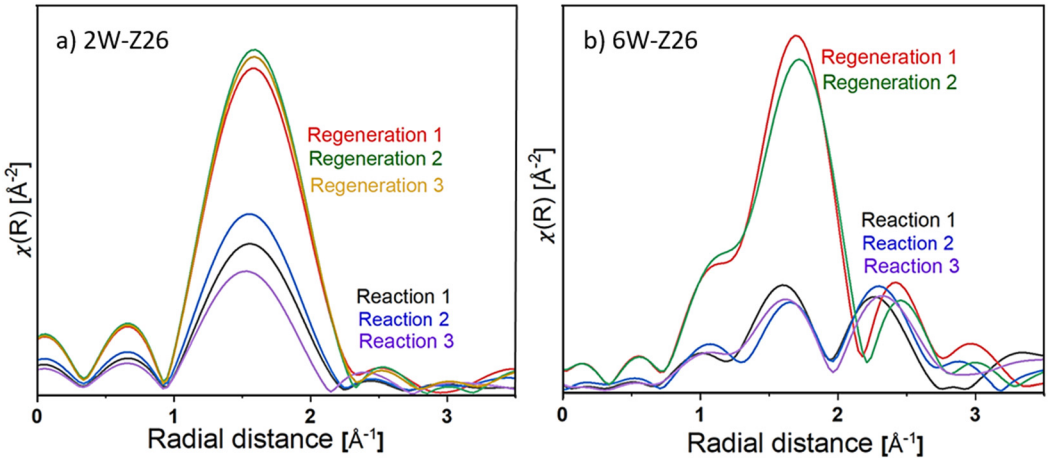

Fig. 10 W L_3-edge FT-EXAFS spectra for the 2W-Z26 and 6W-Z26 catalysts after different reaction (88.2% CH_4/11.8% He flow at 750 °C) and regeneration (dry air flow at 700 °C) cycles. The curves are obtained in the 2.3–7.8 $Å^{-1}$ k-space using a Hanning window.

Open Access Article. Published on 22 March 2023. Downloaded on 2/20/2026 7:25:29 PM.
This article is licensed under a Creative Commons Attribution-NonCommercial 3.0 Unported Licence.

difference between the two catalysts is the emergence of a peak around 2.3 Å for 6W-Z26 (Fig. 10). The comparison of the continuous Cauchy wavelet transforms (WT-EXAFS) applied on the 6W-Z26 EXAFS spectra obtained during the reaction to the known WC reference seems to show that this contribution at 2.3 Å is probably associated with the formation of tungsten carbide bonds W–C during the reaction. The presence of both tungsten-oxo and carburized tungsten species may indicate that the tungsten-oxo particles (W^{6+}) present in the fresh catalyst are partially carburized after contact with CH_4 during the reaction. Considering the previous studies performed on Mo/HZSM-5 catalysts,[65–67] it could be stated that the formation of tungsten carbide species may occur on 6W-Z26 samples during the first stages of the reaction, and these serve as an active phase giving the typical MDA activity which we discussed in previous sections. Overall, these analyses corroborate that there might be different active W sites in terms of structure and oxidation state depending on the tungsten loading. Also, it is possible that structural changes in ZSM-5 support during reaction–regeneration cycles play key roles in the re-dispersion and re-orientation of W sites, which leads to enhanced/declined overall MDA activity depending on the initial W loading (see discussions in previous sections).

Conclusions

In this study, we examined the W-loaded ZSM-5 catalysts from a different perspective than the previous studies in the literature. Besides showing that W activation is more demanding than activation of Mo, and that Mo is a better aromatization catalyst in general; we revealed that W dispersion/distribution on the zeolite is very critical through high-temperature reaction–regeneration cycles. Our results clearly indicate that if W–zeolite interaction and zeolite acidity can be tuned, it would be a promising alternative to replace Mo for MDA reactions. In addition to this, *via operando* XAS analyses, we found the existence of two different active tungsten species (partially reduced tungsten sites and carburized tungsten sites) on W loaded ZSM-5 catalysts. As discussed in the introduction, there was no consensus on the oxidation state of active W species in the MDA literature up to this study. Future endeavours in this field should be fully understanding the structure of these active W species and unravelling the zeolite–tungsten interaction thoroughly.

Experimental methods

Catalyst preparation and characterization

All W and Mo catalysts were prepared *via* incipient wetness impregnation unless otherwise stated, using $(NH_4)_6H_2W_{12}O_{40}{\cdot}xH_2O$ and $(NH_4)_6Mo_7O_{24}{\cdot}4H_2O$ as precursors, respectively. The details about catalyst preparation and catalyst characterization are presented in ESI.†

Catalytic activity tests

All the catalytic performance tests (reaction–regeneration cycles) were conducted in a fixed-bed reactor setup provided by PID Eng & Tech at atmospheric pressure and corresponding temperatures (please see the further details in ESI†). Methane conversion-% (1), product yield-% (2), total yield-% (not including CO and CO_2) (3), H_2 flow at the outlet (ml min^{-1} at STP) (4), and product formation rate per metal atom (turnover frequencies, TOFs) (5) were calculated as follows:

$$X_{CH_4} = \frac{F_{CH_4,in} - F_{CH_4,out}}{F_{CH_4,in}} \times 100 \quad (1)$$

$$Y_x = \frac{F_{x,out} \times (C \text{ number of } x)}{F_{CH_4,in}} \times 100 \quad (2)$$

$$Y_{total} = \sum_{\text{All } x \text{ except } CO,CO_2} Y_x \quad (3)$$

$$F_{H_2,out} = y_{H_2,out} \times F_{total,out} \quad (4)$$

$$TOF_X = \frac{F_{x,out}}{\text{mmoles of metal in the corresponding catalyst}} \quad (5)$$

For *operando* XAS experiments, please see the ESI.†

Author contributions

J. G. conceived, designed and supervised the project together with M. Ç. who prepared the catalysts and performed the catalytic experiments, and most of the characterizations. A. N., A. A. T., J. L. H., and S. O. C. were responsible for the XAS characterization, data analyses and interpretations. S. A. F. N. and L. C. performed the advanced DFT calculations. Solid-state NMR experiments and analyses were carried out by S. C. and J. R. M., A. D., G. S., and T. S. were responsible for the XRD-refinement analysis, XPS experiments, and NH_3-TPD data acquisition, respectively. The manuscript was drafted by M. Ç. and J. G. with input from all the authors.

Conflicts of interest

There are no conflicts to declare.

Acknowledgements

Funding for this work was provided by King Abdullah University of Science and Technology (KAUST). Also, we would like to thank Söhrab Askarli, Qingxiao Wang, Eganathan Kaliyamoorthy and Büşra Dereli for their supports in zeolite-steaming experiments, HAADF-STEM imaging, ICP-OES analysis, and DFT-calculations, respectively. We acknowledge the European Synchrotron Radiation Facility for the provision of synchrotron radiation facilities, and we would like to thank Eric Lahera for assistance in using beamline BM30.

Open Access Article. Published on 22 March 2023. Downloaded on 2/20/2026 7:25:29 PM.
This article is licensed under a Creative Commons Attribution-NonCommercial 3.0 Unported Licence.

References

1 M. Saunois, A. R. Stavert, B. Poulter, P. Bousquet, J. G. Canadell, R. B. Jackson, P. A. Raymond, E. J. Dlugokencky and S. Houweling, *Earth Syst. Sci. Data*, 2020, **12**, 1561–1623.
2 G. Zichittella and J. Pérez-Ramírez, *Chem. Soc. Rev.*, 2021, **50**, 2984–3012.
3 L. Wang, L. Tao, M. Xie, G. Xu, J. Huang and Y. Xu, *Catal. Lett.*, 1993, **21**, 35–41.
4 D. Kiani, S. Sourav, Y. Tang, J. Baltrusaitis and I. E. Wachs, *Chem. Soc. Rev.*, 2021, **50**, 1251–1268.
5 S. Ma, X. Guo, L. Zhao, S. Scott and X. Bao, *J. Energy Chem.*, 2013, **22**, 1–20.
6 M. Çağlayan, A. Lucini Paioni, E. Abou-Hamad, G. Shterk, A. Pustovarenko, M. Baldus, A. D. Chowdhury and J. Gascon, *Angew. Chem., Int. Ed.*, 2020, **59**, 16741–16746.
7 I. Vollmer, N. Kosinov, Á. Szécsényi, G. Li, I. Yarulina, E. Abou-Hamad, A. Gurinov, S. Ould-Chikh, A. Aguilar-Tapia, J. L. Hazemann, E. Pidko, E. Hensen, F. Kapteijn and J. Gascon, *J. Catal.*, 2019, **370**, 321–331.
8 M. Agote-Arán, R. E. Fletcher, M. Briceno, A. B. Kroner, I. V. Sazanovich, B. Slater, M. E. Rivas, A. W. J. Smith, P. Collier, I. Lezcano-González and A. M. Beale, *ChemCatChem*, 2020, **12**, 294–304.
9 N. K. Razdan, A. Kumar, B. L. Foley and A. Bhan, *J. Catal.*, 2020, **381**, 261–270.
10 N. Kosinov, F. J. A. G. Coumans, E. A. Uslamin, A. S. G. Wijpkema, B. Mezari and E. J. M. Hensen, *ACS Catal.*, 2017, **7**, 520–529.
11 T. Shoinkhorova, T. Cordero-Lanzac, A. Ramirez, S. H. Chung, A. Dokania, J. Ruiz-Martinez and J. Gascon, *ACS Catal.*, 2021, **11**, 3602–3613.
12 M. Guisnet, N. S. Gnep, D. Aittaleb and Y. J. Doyemet, *Appl. Catal., A*, 1992, **87**, 255–270.
13 E. Le Roux, M. Taoufik, C. Copéret, A. De Mallmann, J. Thivolle-Cazat, J. M. Basset, B. M. Maunders and G. J. Sunley, *Angew. Chem., Int. Ed.*, 2005, **44**, 6755–6758.
14 S. Lwin, Y. Li, A. I. Frenkel and I. E. Wachs, *ACS Catal.*, 2016, **6**, 3061–3071.
15 I. Dellien, F. M. Hall and L. G. Hepler, *Chem. Rev.*, 1976, **76**, 283–310.
16 N. N. Greenwood and A. Earnshaw, *Chemistry of the Elements*, Elsevier, 2nd edn, 1997.
17 M. Çağlayan, A. L. Paioni, B. Dereli, G. Shterk, I. Hita, E. Abou-Hamad, A. Pustovarenko, A.-H. Emwas, A. Dikhtiarenko, P. Castaño, L. Cavallo, M. Baldus, A. D. Chowdhury and J. Gascon, *ACS Catal.*, 2021, **11**, 11671–11684.
18 N. Kosinov, F. J. A. G. Coumans, G. Li, E. Uslamin, B. Mezari, A. S. G. Wijpkema, E. A. Pidko and E. J. M. Hensen, *J. Catal.*, 2017, **346**, 125–133.
19 G. Plazenet, E. Payen, J. Lynch and B. Rebours, *J. Phys. Chem. B*, 2002, **106**, 7013–7028.
20 J. Yang, D. Ma, F. Deng, Q. Luo, M. Zhang, X. Bao and C. Ye, *Chem. Commun.*, 2002, 3046–3047.
21 W. Ding, G. D. Meitzner, D. O. Marler and E. Iglesia, *J. Phys. Chem. B*, 2001, **105**, 3928–3936.
22 M. A. Abedin, S. Kanitkar and J. J. Spivey, *MRS Adv.*, 2020, 3407–3417.
23 J. Yang, F. Deng, M. Zhang, Q. Luo and C. Ye, *J. Mol. Catal. A: Chem.*, 2003, **202**, 239–246.
24 B. M. Weckhuysen, D. Wang, M. P. Rosynek and J. H. Lunsford, *J. Catal.*, 1998, **175**, 338–346.
25 S.-T. Wong, Y. Xu, L. Wang, S. Liu, G. Li, M. Xie and X. Guo, *Catal. Lett.*, 1996, **38**, 39–43.
26 B. M. Weckhuysen, D. Wang, M. P. Rosynek and J. H. Lunsford, *J. Catal.*, 1998, **175**, 347–351.
27 X. Xu, F. Faglioni and W. A. Goddard, *J. Phys. Chem. A*, 2002, **106**, 7171–7176.
28 V. V. Kozlov, V. I. Zaikovskii, A. V. Vosmerikov, L. L. Korobitsyna and G. V. Echevskii, *Kinet. Catal.*, 2008, **49**, 117–121.
29 J. L. Zeng, Z. T. Xiong, H. Bin Zhang, G. D. Lin and K. R. Tsai, *Catal. Lett.*, 1998, **53**, 119–124.
30 S. Lwin, Y. Li, A. I. Frenkel and I. E. Wachs, *ACS Catal.*, 2016, **6**, 3061–3071.
31 E. I. Ross-Medgaarden and I. E. Wachs, *J. Phys. Chem. C*, 2007, **111**, 15089–15099.
32 M. A. Alvarez-Merino, F. Carrasco-Marín, J. L. G. Fierro and C. Moreno-Castilla, *J. Catal.*, 2000, **192**, 363–373.
33 T. Kim, A. Burrows, C. J. Kiely and I. E. Wachs, *J. Catal.*, 2007, **246**, 370–381.
34 A. A. Costa, P. R. S. Braga, J. L. De MacEdo, J. A. Dias and S. C. L. Dias, *Microporous Mesoporous Mater.*, 2012, **147**, 142–148.
35 A. Guntida, K. Suriye, J. Panpranot and P. Praserthdam, *Catal. Today*, 2020, **358**, 354–369.
36 N. Liu, S. Ding, Y. Cui, N. Xue, L. Peng, X. Guo and W. Ding, *Chem. Eng. Res. Des.*, 2013, **91**, 573–580.
37 A. I. Olivos-Suarez, À. Szécsényi, E. J. M. Hensen, J. Ruiz-Martinez, E. A. Pidko and J. Gascon, *ACS Catal.*, 2016, **6**, 2965–2981.
38 X. Gong, M. Çağlayan, Y. Ye, K. Liu, J. Gascon and A. Dutta Chowdhury, *Chem. Rev.*, 2022, **122**, 14275–14345.
39 M. Weil and W. D. Schubert, *The Beautiful Colours of Tungsten Oxides*, London, 2013.
40 J. Goetze, F. Meirer, I. Yarulina, J. Gascon, F. Kapteijn, J. Ruiz-Martínez and B. M. Weckhuysen, *ACS Catal.*, 2017, **7**, 4033–4046.
41 S. V. Konnov, V. S. Pavlov, P. A. Kots, V. B. Zaytsev and I. I. Ivanova, *Catal. Sci. Technol.*, 2018, **8**, 1564–1577.
42 S. Kumar, A. K. Sinha, S. G. Hegde and S. Sivasanker, *J. Mol. Catal. A: Chem.*, 2000, **154**, 115–120.
43 S. M. T. Almutairi, B. Mezari, E. A. Pidko, P. C. M. M. Magusin and E. J. M. Hensen, *J. Catal.*, 2013, **307**, 194–203.
44 C. J. Heard, L. Grajciar, F. Uhlík, M. Shamzhy, M. Opanasenko, J. Čejka and P. Nachtigall, *Adv. Mater.*, 2020, **32**, 1–29.
45 A. R. Maag, G. A. Tompsett, J. Tam, C. A. Ang, G. Azimi, A. D. Carl, X. Huang, L. J. Smith, R. L. Grimm, J. Q. Bond and M. T. Timko, *Phys. Chem. Chem. Phys.*, 2019, **21**, 17880–17892.

Open Access Article. Published on 22 March 2023. Downloaded on 2/20/2026 7:25:29 PM.
This article is licensed under a Creative Commons Attribution-NonCommercial 3.0 Unported Licence.

46 A. S. Al-Dughaither and H. De Lasa, *Ind. Eng. Chem. Res.*, 2014, **53**, 15303–15316.
47 E. I. Ross-Medgaarden and I. E. Wachs, *J. Phys. Chem. C*, 2007, **111**, 15089–15099.
48 C. H. L. Tempelman and E. J. M. Hensen, *Appl. Catal., B*, 2015, **176–177**, 731–739.
49 A. Aguilar-Tapia, S. Ould-Chikh, E. Lahera, A. Prat, W. Delnet, O. Proux, I. Kieffer, J. M. Basset, K. Takanabe and J. L. Hazemann, *Rev. Sci. Instrum.*, 2018, **89**, 035109.
50 Solid Spectroscopy Hosting Architecture of Databases and Expertise | SSHADE, **https://www.sshade.eu/**, (accessed 18 January 2023).
51 B. C. Bostick, J. Sun, J. D. Landis and J. L. Clausen, *Environ. Sci. Technol.*, 2018, **52**, 1045–1053.
52 J. L. Clausen, B. C. Bostick, A. Bednar, J. Sun and J. D. Landis, *Tungsten Speciation in Firing Range Soils*, U.S. Army Environmental Command, 5179 Hoadley Road, Aberdeen Proving Ground, MD, 2021, **https://apps.dtic.mil/sti/pdfs/ADA535133.pdf**.
53 S. Yamazoe, Y. Hitomi, T. Shishido and T. Tanaka, *J. Phys. Chem. C*, 2008, **112**, 6869–6879.
54 F. Hilbrig, H. E. Göbel, H. Knözinger, H. Schmelz and B. Lengeler, *J. Phys. Chem.*, 1991, **95**, 6973–6978.
55 X. Carrier, E. Marceau, H. Carabineiro, V. Rodríguez-González and M. Che, *Phys. Chem. Chem. Phys.*, 2009, **11**, 7527–7539.
56 T. Witoon, P. Kidkhunthod, M. Chareonpanich and J. Limtrakul, *Chem. Eng. J.*, 2018, **348**, 713–722.
57 C. R. VanderSchee, D. Kuter, A. M. Bolt, F. C. Lo, R. Feng, J. Thieme, Y. Chen, K. Chen-Wiegart, G. Williams, K. K. Mann and D. S. Bohle, *Commun. Chem.*, 2018, **1**, 8.
58 W. Zhou, E. I. Ross-Medgaarden, W. v. Knowles, M. S. Wong, I. E. Wachs and C. J. Kiely, *Nat. Chem.*, 2009, **1**, 722–728.
59 S. Li, H. Zhou, C. Jin, N. Feng, F. Liu, F. Deng, J. Q. Wang, W. Huang, L. Xiao and J. Fan, *J. Phys. Chem. C*, 2014, **118**, 6283–6290.
60 W. Zhou, I. E. Wachs and C. J. Kiely, *Curr. Opin. Solid State Mater. Sci.*, 2012, 16.
61 J. Kowalska and S. DeBeer, *Biochim. Biophys. Acta, Mol. Cell Res.*, 2015, **1853**, 1406–1415.
62 Y. Kou, B. Zhang, J. Z. Niu, S. Ben Li, H. L. Wang, T. Tanaka and S. Yoshida, *J. Catal.*, 1998, **173**, 399–408.
63 A. Kuzmin and J. Purans, *Radiat. Meas.*, 2001, **33**, 583–586.
64 L. Gracia, V. M. Longo, L. S. Cavalcante, A. Beltrn, W. Avansi, M. S. Li, V. R. Mastelaro, J. A. Varela, E. Longo and J. Andrés, *J. Appl. Phys.*, 2011, **110**, 043501.
65 N. Wang, X. Dong, L. Liu, D. Cai, Q. Cheng, J. Wang, Y. Hou, A. H. Emwas, J. Gascon and Y. Han, *Cell Rep. Phys. Sci.*, 2021, **2**, 100309.
66 N. Kosinov, A. S. G. Wijpkema, E. Uslamin, R. Rohling, F. J. A. G. Coumans, B. Mezari, A. Parastaev, A. S. Poryvaev, M. V. Fedin, E. A. Pidko and E. J. M. Hensen, *Angew. Chem., Int. Ed.*, 2018, **57**, 1016–1020.
67 N. Kosinov, E. A. Uslamin, F. J. A. G. Coumans, A. S. G. Wijpkema, R. Y. Rohling and E. J. M. Hensen, *ACS Catal.*, 2018, **8**, 8459–8467.
68 NIST Chemistry WebBook, **https://webbook.nist.gov/chemistry/**, (accessed 13 June 2022).
69 PubChem - National Library of Medicine, **https://pubchem.ncbi.nlm.nih.gov/**, (accessed 13 June 2022).

 This journal is © The Royal Society of Chemistry 2023